

WVMS: MEASURING WATER VAPOR IN THE MIDDLE ATMOSPHERE

G.E. Nedoluha, R.M. Bevilacqua, R.M. Gomez,
and B.C. Hicks

Remote Sensing Division

Introduction: The Naval Research Laboratory has a long history of measuring water vapor in the middle atmosphere. This is the region of the atmosphere above the troposphere (~0 to 10 km), which includes the stratosphere (~10 to 50 km) and the mesosphere (~50 to 90 km). In the early 1960s, there was still considerable uncertainty over how much water the stratosphere contained. Some measurements showed that it was “wet,” with ~100 water vapor molecules for every million molecules (100 ppmv), while others showed that it was “dry,” with ~4 to 5 ppmv. NRL’s John Mastenbrook¹ launched frost-point hygrometers on balloons up to altitudes of ~28 km, and is credited with finally resolving this controversy in favor of the “dry” stratosphere. This program continued at the Naval Research Laboratory from 1964 until 1979.

Water vapor measurements in the middle atmosphere are important for several reasons. First, water vapor is the primary source of the OH radical and other hydrogen compounds, and is therefore important in ozone chemistry. In addition, water vapor entering the stratosphere is extremely sensitive to temperatures at the tropical tropopause, and is therefore relevant to our understanding of how and where air rises from the troposphere into the stratosphere.

Finally, because water vapor is an important greenhouse gas, the amount of water vapor in the atmosphere is extremely relevant to the global warming problem.

WVMS: The Water Vapor Millimeter-wave Spectrometer (WVMS) instruments (Fig. 1) make spectral measurements near 22 GHz, and thereby provides measurements of the water vapor profile from 40 to 80 km. The goal of this project is to provide the first continuous record of water vapor in the middle atmosphere using ground-based radiometers. All of the instruments have provided nearly continuous data records during their period of operation. The data from Table Mountain, California, covers the period from May 1993 to November 1997. The measurements from Lauder, New Zealand, cover the period from November 1992 to May 1993, and from January 1994 to the present. A third instrument was installed at Mauna Loa, Hawaii, in February 1996, and has been providing continuous data since that time. The instruments are all operated remotely from the Naval Research Laboratory, with calibration and emergency support provided by on-site staff. Figure 2 shows the data record from all three sites.

The instruments are installed at sites of the international Network for the Detection of Stratospheric Change (NDSC). NDSC is a set of high-quality remote-sounding research stations for observing and understanding the physical and chemical state of the stratosphere. The WVMS instruments provide the sole source of middle atmospheric water vapor data from these sites.



FIGURE 1

The WVMS instrument at Mauna Loa, Hawaii. The high altitude of this site makes it ideal for microwave measurements of the middle atmosphere.

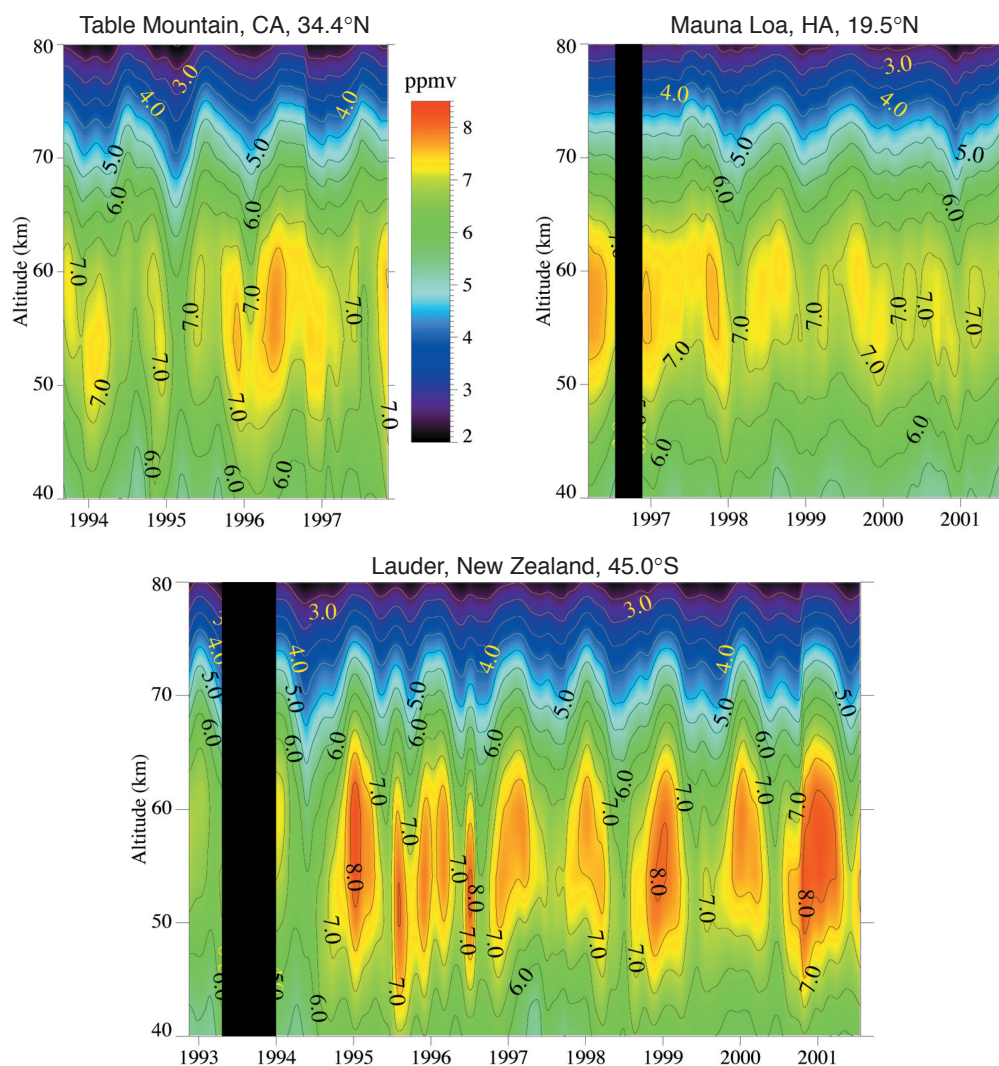


FIGURE 2

Full data record from the three sites where WVMS instruments have been deployed. Note the seasonal cycles at all three sites. Because the Lauder, NZ, site is farthest from the equator, it shows the most pronounced annual variation.

Increasing Middle Atmospheric Water Vapor: There has been an observed increase in middle atmospheric water vapor both on decadal and multi-decadal timescales. The WVMS measurements played an important role in documenting the large increase (~2%/year) in middle atmospheric water vapor that was observed in the early 1990s.² This increase is thought to be related to the eruption of Mount Pinatubo in 1991, but the precise mechanism that caused the increase is still not understood. In addition to the increase in the early 1990s, there are measurements that suggest a longer term but somewhat slower increase in middle atmospheric water vapor that dates back to the 1950s.³ Although some of this long-term increase can be attributed to the effects of global increases in methane on water vapor, the observed increase is too large to be attrib-

uted entirely to this mechanism. The magnitude of the observed increases in middle atmospheric water vapor, the difficulty of pinpointing the causes of these increases, and the importance of such increases to ozone chemistry and global warming all highlight the importance of maintaining these continuous measurements.

[Sponsored by NASA]

References

- ¹ H.J. Mastenbrook, "Water Vapor Distribution in the Stratosphere and High Troposphere," *J. Atmos. Sci.* **25**, 299-311 (1968).
- ² G.E. Nedoluha et al., "Increases in Middle Atmospheric Water Vapor as Observed by HALOE and the Ground-based Water Vapor Millimeter-wave Spectrometer from 1991-1997," *J. Geophys. Res.* **103**, 3531-3542 (1998).
- ³ K.H. Rosenlof et al., "Stratospheric Water Vapor Increases over the Past Half-century," *Geophys. Res. Lett.* **28**, 1195-1198 (2001).

ATMOSPHERIC STRUCTURE, SEA STATE, AND RADAR PROPAGATION CONDITIONS ASSOCIATED WITH AN ISLAND WAKE

S.D. Burk,¹ T. Haack,¹ L.T. Rogers,² L.J. Wagner,² and P. Wittmann³

¹Marine Meteorology Division

²Space and Naval Warfare Systems Center

³Fleet Numerical Meteorology and Oceanography Center

Introduction: Microwave and millimeter-wave propagation near the ocean surface can be greatly impacted by the atmospheric refractivity profile and the sea state. Previous studies¹ have dealt with ducts associated with inversions at the boundary layer top, whereas surface layer ducts (<30 m generally) are of primary importance to this study. Large negative gradients of water vapor near the sea surface often create sharp refractivity gradients and an “evaporation duct.” Evaporation duct height δ is the height at which the refractivity gradient no longer acts to trap energy.

During radar performance tests on 3 December 1999 leeward of Kauai, Hawaii, observations aboard the USS *O’Kane* indicated anomalous azimuthal variability in the clutter distribution postulated to be due to an island wake. To test this hypothesis, the NRL Coupled Ocean/Atmosphere Mesoscale Prediction System (COAMPS) is used for idealized simulations of initially homogeneous, stratified atmospheric flow perturbed by the island. The factors controlling the formation, size, and stability of island wakes, as well as the wake impact on refractivity are investigated. Subsequently, a real data COAMPS forecast is made for the period of the *O’Kane* observations. Because a roughened sea state can enhance the backscattered

radar clutter, we also use the Wave Watch III (WW3) numerical ocean wave model. Atmospheric wind and refractivity fields from COAMPS and sea state from WW3 provide input to an electromagnetic (EM) propagation code and to a sea clutter model. The propagation model generates values of propagation loss, while the clutter model computes normalized radar cross-section and modeled clutter power for comparison to the observed radar return.

Idealized Island Wake Simulations: From a benchmark simulation using a 1-km resolution terrain database, results are compared to simulations in which the island height h_m is varied by factors of 1/2, 3/4, and 2. Based on linear theory of stratified flow and shallow-water model studies, the non-dimensional mountain height $\mathbf{h} = Nh_m/U$ is an important control parameter for describing the dynamics. Other important control factors are mountain shape and aspect ratio, surface drag, and for single-layer flow, layer depth relative to h_m . Buoyancy frequency N and wind speed U often are taken as uniform with height, but here we address variable stratification. N and U are averaged from the surface to twice the mountain height when computing \mathbf{h} , thereby encompassing a representative depth of the perturbed flow. In the benchmark simulation, $h_m = 1.3$ km and $\mathbf{h} = 1.4$. The theory for uniform stratification² indicates that straight wakes are to be expected for the island configuration, drag, and \mathbf{h} of this simulation. However, a meandering wake actually develops (Fig. 3), indicating that nonuniform stratification alters wake stability. Figure 3(a) shows upstream blocking and deceleration of the near-surface wind, with strong acceleration on the island flanks producing pronounced lateral shear across the meandering, low wind speed wake. Figure 3(b) shows that the wake is connected to a sharply descending leeside mountain wave.

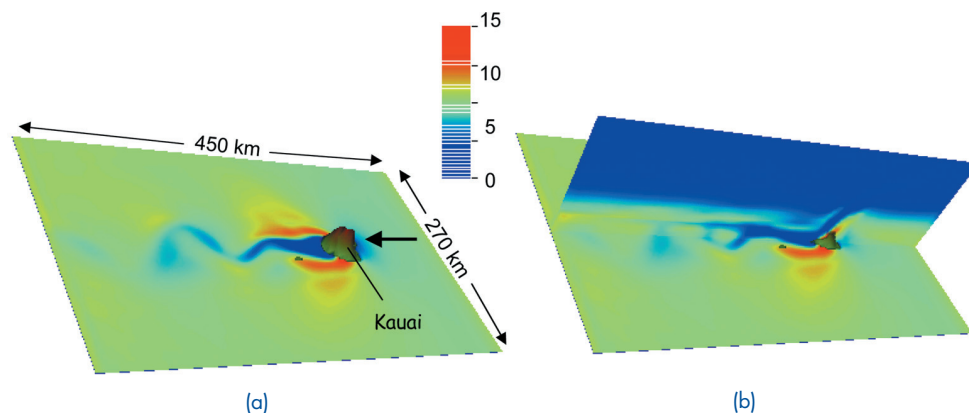


FIGURE 3

(a) Near-surface wind speed (color bar in m s^{-1}) from the benchmark case; (b) same as (a), with a vertical cross section extending from the surface to 3 km.

With $h = 0.49$ ($1/2 h_m$ case), only a small pair of counter-rotating vortices develop; with $h = 0.87$ ($3/4 h_m$), a long straight wake forms leeward of the island. When $h = 3.5$ ($2 h_m$), a long, periodic train of von Kármán vortices is shed from the island. The primary mechanism generating these vortices in this case appears to be hydraulic jump features occurring on the island flanks, with the flow being strongly blocked and deflected around the mountain and no pronounced mountain wave over the crest.

Real Data Case: Figure 4(a) shows that the model's evaporation duct height in the real data case contains a clear island wake signature, with a minimum $\delta \approx 4$ m in the wake and maximum $\delta \approx 14$ m

outside the wake. Wave height and direction from WW3 appear in Fig. 4(b), showing a wake in sea state. The observed clutter map from the USS *O'Kane* appears in Fig. 5(a), while Fig. 5(b) shows the modeled clutter map. Both maps depict enhanced ranges of clutter north-south, which coincides with the higher wind speeds and larger δ values. The clutter power falls off more sharply along the direction of the low wind speed (and small δ) wake.

Conclusions: The modeled trend of wake structure and stability with increasing nondimensional mountain height—from no wake, to a long straight wake, to a meandering wake, and finally to periodically shed vortices—is *qualitatively* similar to that

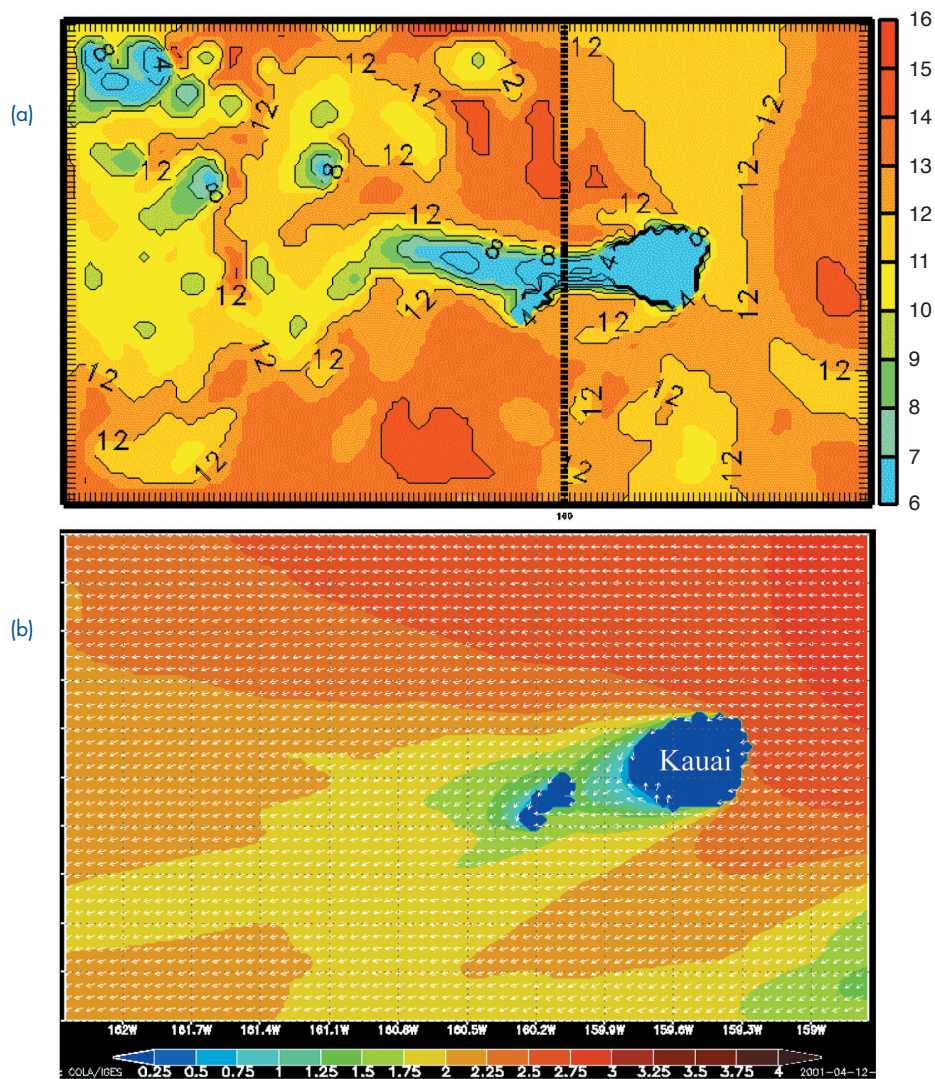


FIGURE 4
(a) COAMPS real data forecast of evaporation duct height (m); and (b) WW3 forecast of wave height (color bar in m) and direction (vectors). Both (a) and (b) are for 0600 UTC 3 December 1999.

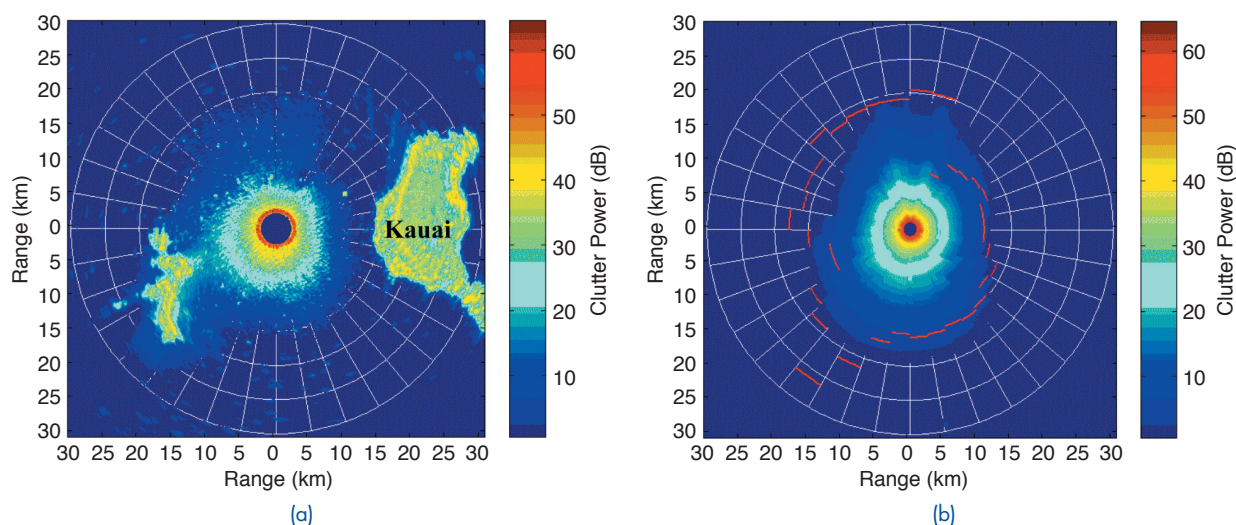


FIGURE 5

(a) Observed clutter map from the USS O'Kane radar on 3 December 1999 with islands of Kauai and Niihau; (b) modeled clutter map computed from linkage of diverse model systems described in text.

found with models having uniform stratification. Stratification, however, is found to *quantitatively* alter the critical h values defining transitions between wake regimes. This study demonstrates that an island wake, through its impact on the atmospheric refractivity field and the sea state, can account for anomalies observed in radar clutter pattern. The linkage of the diverse model systems presented here is expected to have wide application to other littoral environments having mesoscale inhomogeneities.

[Sponsored by ONR]

References

- ¹T. Haack and S.D. Burk, "Summertime Marine Refractivity Conditions along Coastal California," *J. Appl. Meteor.* **40**, 673-687 (2001).
- ²R.B. Smith, A.C. Gleason, P.A. Gluhosky, and V. Grubiai, "The Wake of St. Vincent," *J. Atmos. Sci.* **54**, 606-623 (1997). ■

VARIABILITY OF ATMOSPHERIC FORECAST ERROR SENSITIVITY 1996-2000

C.A. Reynolds and R. Gelaro*
Marine Meteorology Division
 *Current affiliation: NASA

Introduction: The Navy Operational Global Atmospheric Prediction System (NOGAPS) operational 2-day Northern Hemisphere extratropical forecast error sensitivity to changes in the initial conditions has been calculated by NRL on a daily basis since October 1996.¹ This 4-year archive of daily adjoint sensitivity calculations provides an opportu-

nity to diagnose the locations where, on average, initial-condition errors have had the largest impact on the forecast errors. The fortuitous occurrence of large variations in the El Niño cycle during this period allows us to examine interannual variations as well as interseasonal variations in predictability.

We use the adjoint of the NOGAPS forecast model to diagnose the sensitivity of the forecast error to changes in the initial conditions in a mathematically rigorous way. The adjoint integration that produces the forecast sensitivity does not contain moist physics, although it does contain a simplified representation of boundary layer physics and vertical diffusion.² The sensitivity calculation is based on the dry total energy of the forecast error between 30°N to 90°N and from the surface to approximately 150 hPa. The operational data assimilation system used throughout this period has been a multivariate optimum interpolation scheme. The same version of the forecast and adjoint model was used for the entire 4-year period.

Interannual Variability: We use time-longitude diagrams to concisely illustrate zonal and temporal variations in forecast error and sensitivity. Because the fastest growing perturbations are dominated by potential energy at initial time and kinetic energy at final time, forecast errors are shown in terms of the wind field, while sensitivity is shown in terms of the temperature field. The left-hand panel in Fig. 6 is a time-longitude diagram of the monthly-mean vertically averaged root-mean-square (RMS) wind errors, latitudinally averaged from 30°N to 60°N. A strong seasonal cycle is apparent as well as significant zonal variations during winter. In the

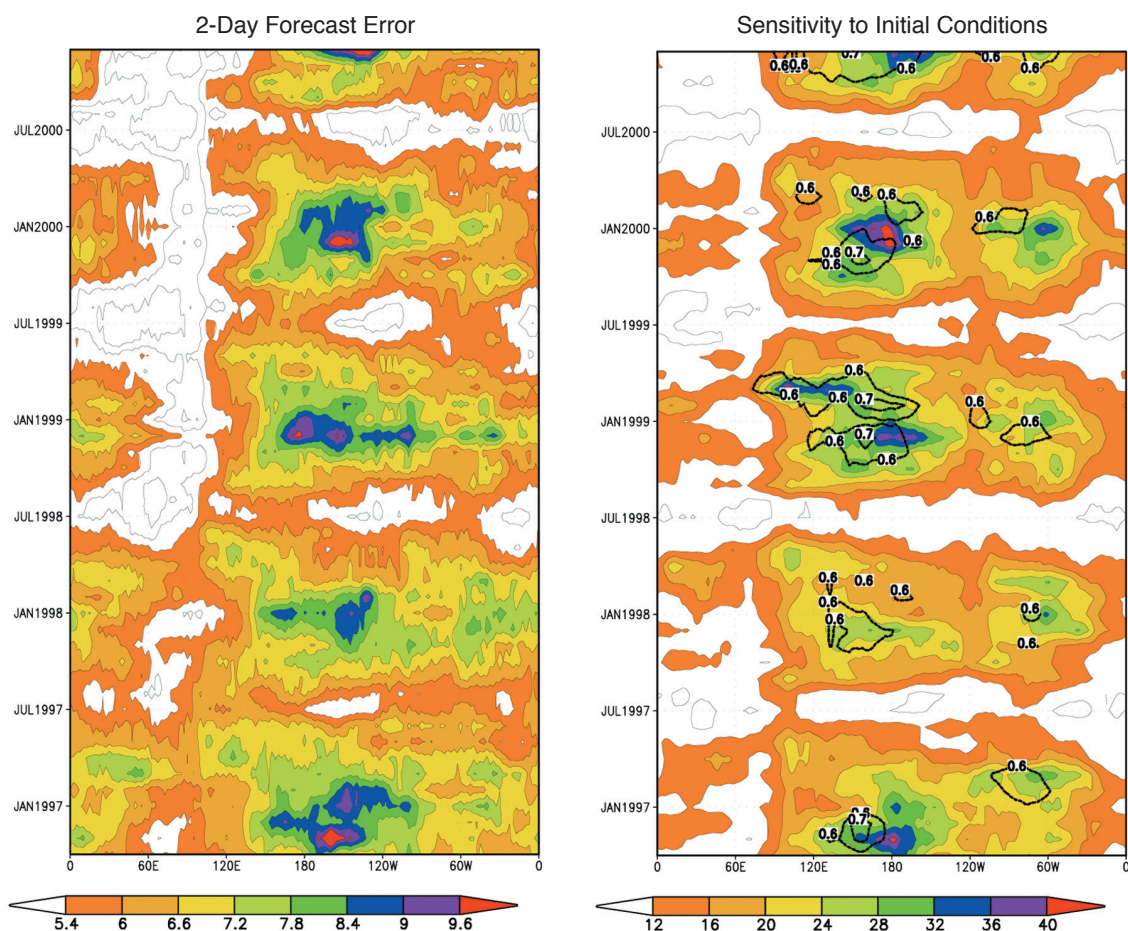


FIGURE 6
Time-longitude diagrams of the vertically averaged 2-day RMS wind error (left) and sensitivity temperature field (right), averaged from 30°N–60°N. The wind error contour interval is 0.6 m s⁻¹; values greater than 5.4 m s⁻¹ are shaded. The temperature sensitivity contour interval is 4 K, with values greater than 12 K shaded. Superimposed on the sensitivity is the Eady index of baroclinic instability, denoted by the thick black line, with contours at 0.6 and 0.7 day⁻¹. (From Ref. 1.)

wintertime, local forecast error maxima correspond roughly to the longitudinal locations of the North Pacific and North Atlantic storm tracks. Note that winter 1997/98 has smaller peak error values over the North Pacific than the other winters.

The right-hand panel in Fig. 6 is a time-longitude diagram of the vertically averaged RMS temperature fields corresponding to the forecast error sensitivity. In general, the interseasonal and interannual variability of the sensitivity is similar to that of the forecast error, although the sensitivity maxima occur upstream (westward) of the forecast error maxima. This is consistent with the fact that, on average, forecast errors propagate eastward with time. The relatively low values of sensitivity during the El Niño winter of 1997/98 over the North Pacific is evidence that this particular winter was intrinsically more predictable than the other winters. This result is consistent with the fact that the Eady index of baroclinic instability, which is a measure of the

potential energy available for conversion to perturbation energy, was also lower during this winter relative to the other winters.

Key Analysis Errors: The adjoint sensitivity of the forecast errors also allows us to diagnose “key” analysis errors (i.e., the components of the analysis errors that grow rapidly and dominate the forecast errors). Figure 7 shows vertical cross sections corresponding to the forecast error and sensitivity fields shown in Fig. 6 for a typical winter month (January 1999). The forecast errors tend to be largest near the jet stream in the upper troposphere, but are most sensitive to upstream changes in the middle-lower troposphere. These results are consistent with our previous findings, which show that rapidly growing perturbations tend to originate in the lower atmosphere, but propagate upward and eastward rapidly as they evolve. These results highlight the necessity of accurate analyses of the lower-tropospheric atmo-

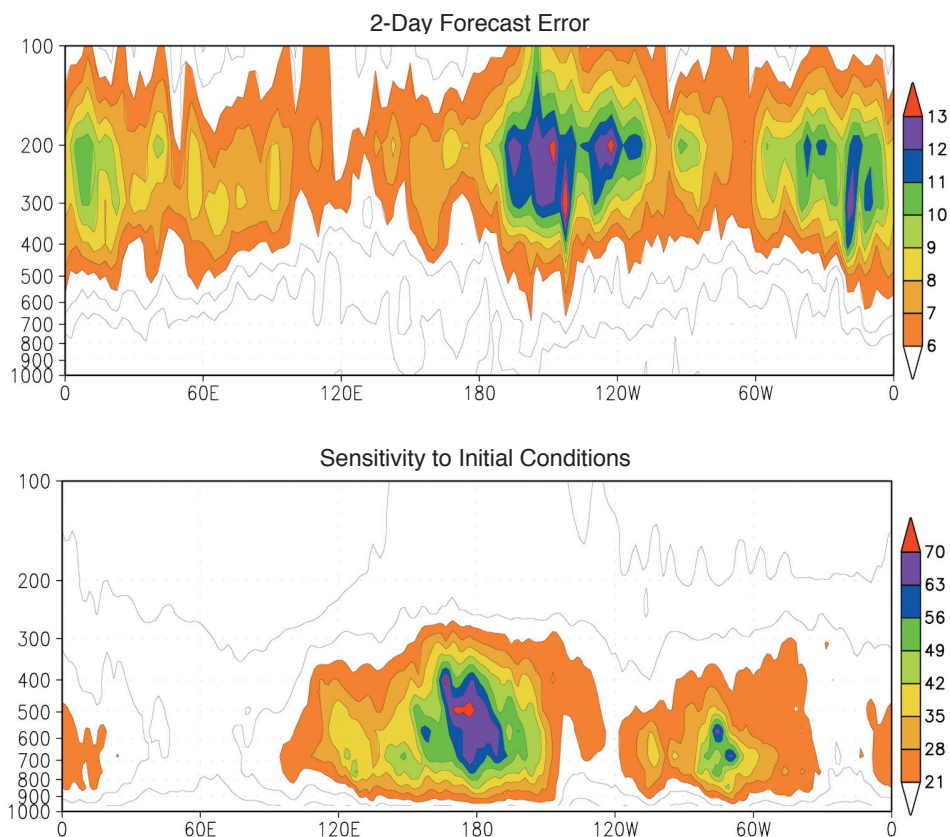


FIGURE 7
Vertical cross sections (pressure-longitude) of the 2-day RMS wind error (top) and sensitivity temperature field (bottom) averaged from 30°N-60°N for December 1999. The wind error contour interval is 1 m s⁻¹; values greater than 6 m s⁻¹ are shaded. The temperature sensitivity contour interval is 7 K, with values greater than 21 K shaded. (From Ref. 1.)

spheric structure over the central North Pacific for accurate forecasts over the eastern North Pacific and North America.

Summary: The results presented here highlight the prominence of wintertime forecast errors and initial condition sensitivity over the North Pacific, a region of vigorous baroclinic activity and relatively few observations. These results confirm the importance of accurate analyses in the middle to lower troposphere. The 4-year time series also provides evidence of significant interannual variability in predictability, indicating that the El Niño winter of

1997/98 appears to have been an anomalously predictable period.

Acknowledgments: Computer resources were provided by the DOD High Performance Computing Program at the NAVO MSRC.
[Sponsored by ONR]

References

- ¹ C.A. Reynolds and R. Gelaro, "Remarks on Northern Hemisphere Forecast Error Sensitivity from 1996 to 2000," *Mon. Wea. Rev.* **129**, 2145-2153 (2001).
- ² T.E. Rosmond, "A Technical Description of the NRL Adjoint Modeling System," NRL/MR/7531/97/7230, Naval Research Laboratory, Monterey, CA, 1997. ■